**Supporting Information**

# Atomic-Level Active Sites of Efficient Imidazolate Frameworks-Derived Nickel Catalysts for $CO_2$ Reduction

Fuping Pan,[a⊥] Hanguang Zhang,[b⊥] Zhenyu Liu,[c⊥] David Cullen,[d] Kexi Liu,[c] Karren More,[d] Gang Wu,[b*] Guofeng Wang,[c*] Ying Li[a*]

[a] J. Mike Walker '66 Department of Mechanical Engineering, Texas A&M University, College Station, Texas 77843, United States

[b] Department of Chemical and Biological Engineering, University at Buffalo, The State University of New York, Buffalo, New York 14260, United States

[c] Department of Mechanical Engineering and Materials Science, University of Pittsburgh, Pittsburgh, Pennsylvania 15261, United States

[d] Materials Science and Technology Division, Oak Ridge National Laboratory, Oak Ridge, Tennessee 37831, United States

[⊥] These authors contributed equally to this work.

*Corresponding authors:

gangwu@buffalo.edu (G. Wu); guw8@pitt.edu (G. Wang); yingli@tamu.edu (Y. Li)

**Catalyst Synthesis**

For the synthesis of Ni-N-C (Ni-N-C-33) catalyst, $Ni(NO_3)_2 \cdot 6H_2O$ (707 mg) and $Zn(NO_3)_2 \cdot 6H_2O$ (1.69 g) were dissolved into 300 mL methanol. A 300 mL of methanol solution of 2-methylimidazole (3.74g) was added into the solution of metal salts above. Then the mixture was kept at 60 °C for 24 h. The resulting precipitant was collected by centrifuging and washing with ethanol for three times. The attained solid was dried at 60 °C under vacuum for 8 h. The dried powder was transferred into an alumina combustion boat, and heat-treated at 1100 °C for 1 h under nitrogen flow in a horizontal tube furnace to obtain the Ni-N-C catalyst. The synthesis of N-C catalyst followed the same procedure except for without the addition of $Ni(NO_3)_2 \cdot 6H_2O$. The different Ni doping contents for Ni-N-C-11 and Ni-N-C-55 were obtained by varying the mole ratio between $Ni^{2+}$ to $Zn^{2+}$ for 0.12:1 and 1.2:1, respectively.

**Catalyst Characterization**

Powder X-ray diffraction patterns of precursors and catalysts were recorded using the Cu Kα X-ray source from diffractometer (Rigaku Ultima IV). The scanning electron microscopy images were collected by a focused ion beam scanning electron microscope (Zeiss Auriga crossbeam). Scanning transmission electron microscope (Nion UltraSTEM U100) equipped with an electron energy loss spectrometer (Gatan Enfina) were used to collect high-resolution transmission electron micrographs, high-angle annular dark-field micrographs and electron energy loss spectra for verifying signals of Ni and N elements. The Renishaw Raman system was employed to obtain the Raman spectra for catalysts with a 514 nm laser and the 50x objective at ambient condition. X-ray photoelectron spectroscopy (Omicron) was conducted to measure the surface composition.

**Electrochemical Measurements**

Electrocatalytic $CO_2RR$ tests were carried out in a two-compartment three-electrode electrochemical cell in $CO_2$-saturated 0.1 M $KHCO_3$ electrolyte (pH=6.8). A Pt mesh and Ag/AgCl

(3M KCl) were used as the counter electrode and reference electrode, respectively. The working electrode was prepared by drop-casting 120 μL of catalyst ink onto carbon paper (1 $cm^2$) with mass loading of 0.6 mg $cm^{-2}$. The ink was prepared by dispersing 3 mg catalyst in mixture solution of 200 μL DI-water, 370 μL ethanol, and 30 μL 5% Nafion solution *via* sonication for 3 h. The working and reference electrodes were placed in the cathode chamber, while counter electrode was placed in the anode chamber, which was separated by a piece of Nafion 115 ionic exchange membrane. The high purity $CO_2$ was introduced in the cathode chamber for 1 h with a flow rate of 34 mL $min^{-1}$ before electrolysis. The gas-phase products were analyzed by using an online gas chromatograph (GC, Fuel Cell GC-2014ATF, Shimadzu) equipped with a thermal conductivity detector (TCD) and a methanizer assisted flame ionization detector (FID). The measured potentials after *i*R compensation were rescaled to the reversible hydrogen electrode by $E$ (RHE) = $E$ (Ag/AgCl) + 0.210 V + 0.0591V×pH.

Faradaic Efficiency (FE) of gas phase product at each applied potential was calculated based on the equation FE = $(z \cdot P \cdot F \cdot V \cdot v_i)/(R \cdot T \cdot j)$, where z is the number of electrons transferred per mole of gas product ($z$ is 2 for CO and $H_2$), $P$ is pressure ($1.01 \times 10^5$ Pa), $F$ is Faraday constant (96500 C $mol^{-1}$), $V$ is the gas flow rate ($5.67\times10^{-7}$ $m^3$ $s^{-1}$), $v_i$ is the volume concentration of gas product determined by GC, $T$ is the temperature (298.15 K), and $R$ is the gas constant (8.314 J $mol^{-1}$ $K^{-1}$). $j$ is the steady-state current at each applied potential. The partial current density for CO and $H_2$ is determined by calculating the total current density multiplied by FE of CO and $H_2$, respectively.

**Computational Method**

Spin-polarized density functional theory (DFT) calculations were performed within the formulism of plane wave basis set and projector augmented wave method, as implemented in the Vienna ab initio simulation package (VASP) code. [1, 2] Electronic exchange and correlation were described within the framework of generalized gradient approximation (GGA) in the form of revised Perdew, Burke and Ernzernhof (RPBE) functionals. [3] A kinetic energy cutoff of 400 eV was used to expand the wave functions. The atomic positions were optimized until the forces were below 0.01 eV/Å

during structural optimization. Two different active sites (Ni−$N_4$-$C_{10}$ and Ni−$N_{2+2}$-$C_8$) were investigate in this work, which atomic structures are shown in Figure S10. The Brillouin zone was sampled using Monkhorst-Pack 4 × 3 × 1 and 4 × 4 × 1 k-point grids for the two active site, respectively. The computational hydrogen electrode method developed by Nørskov was used to calculate the free energy of each intermediate state. [4]

The free energy of $H^+ + e^-$ is calculated by the free energy of $\frac{1}{2}H_2$ at standard state according to the definition of reversible hydrogen electrode (RHE).

The reaction free energy of a chemical is calculated by

$$\Delta G^0 = \Delta E_{DFT} + \Delta E_{ZPE} + \Delta E_{solv} + \Delta H_{0\ to\ T} - T\Delta S$$

where $\Delta E_{DFT}$ is the calculated energy change in DFT, $\Delta E_{ZPE}$ is the zero-point energy correction, $\Delta E_{solv}$ is the solvation energy correction, $\Delta H_{0\ to\ T}$ is the enthalpy change from 0 to T K, and $\Delta S$ is the entropy change. The ZPE corrections were calculated as ZPE = $\sum_i \frac{1}{2} h\nu_i$, where $h$ is Planck's constant and $\nu_i$ is the frequency of the $i$ th vibrational mode of binding molecules. $\Delta H_{0\ to\ T}$ was calculated by the vibrational heat capacity integration $\int_0^T C_p dT$. The entropy terms for gas phase were derived from partition functions and compared with the data from NIST Standard reference database. [5] A solvation effect correction was included by following previously reported values, namely 0.25 eV stabilization of COOH*, 0.1 eV stabilization of CO*. [6] Moreover, a thermodynamic correction of 0.43/0.04 eV for CO2(g)/CO(g) suggested by the previous study was applied to ensure the calculated reaction free energy agrees with the experiments. [7] The corrections and calculated free energy of adsorbed configurations of each species on Ni-N-C active sites were listed in Table S3.

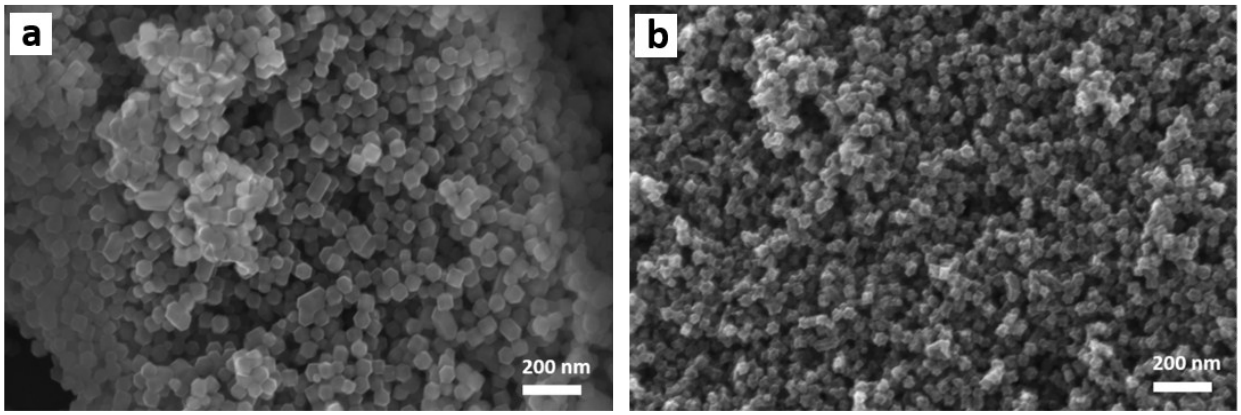


**Fig. S1.** The SEM images of the the ZIF-8 (**a**) and its derived N-C (**b**) catalysts.

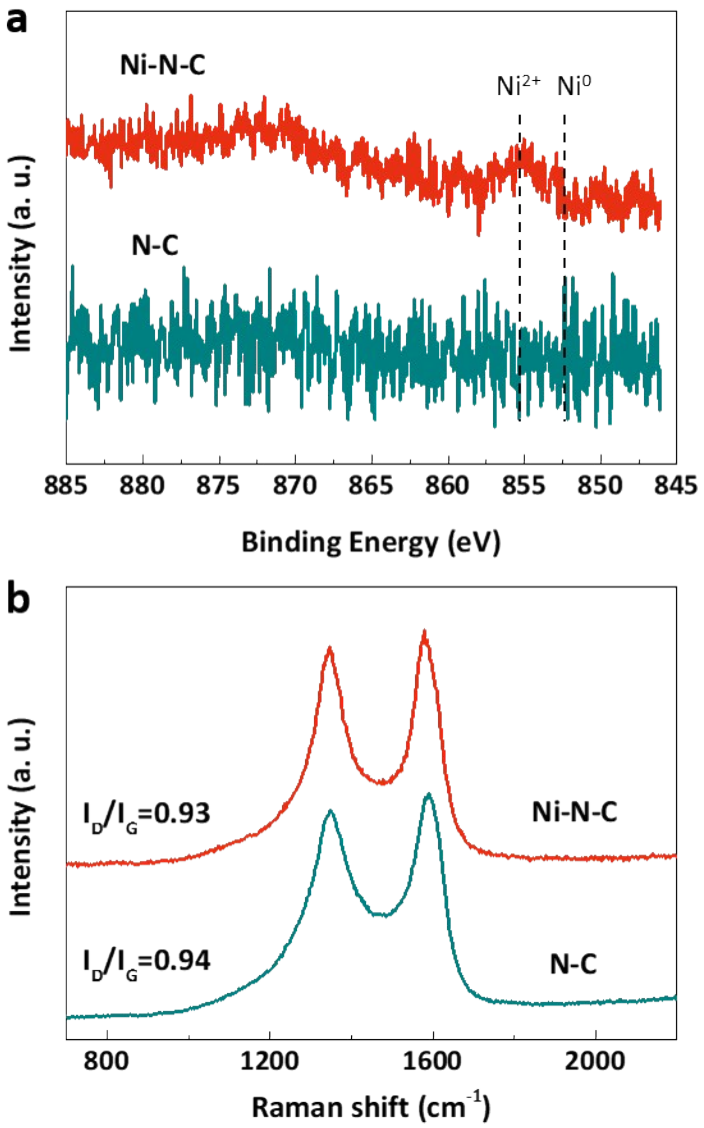


**Fig. S2.** The Ni 2p spectra (a) of high-resolution XPS for Ni-N-C and N-C catalysts; The Raman spectra for Ni-N-C and N-C catalysts (b).

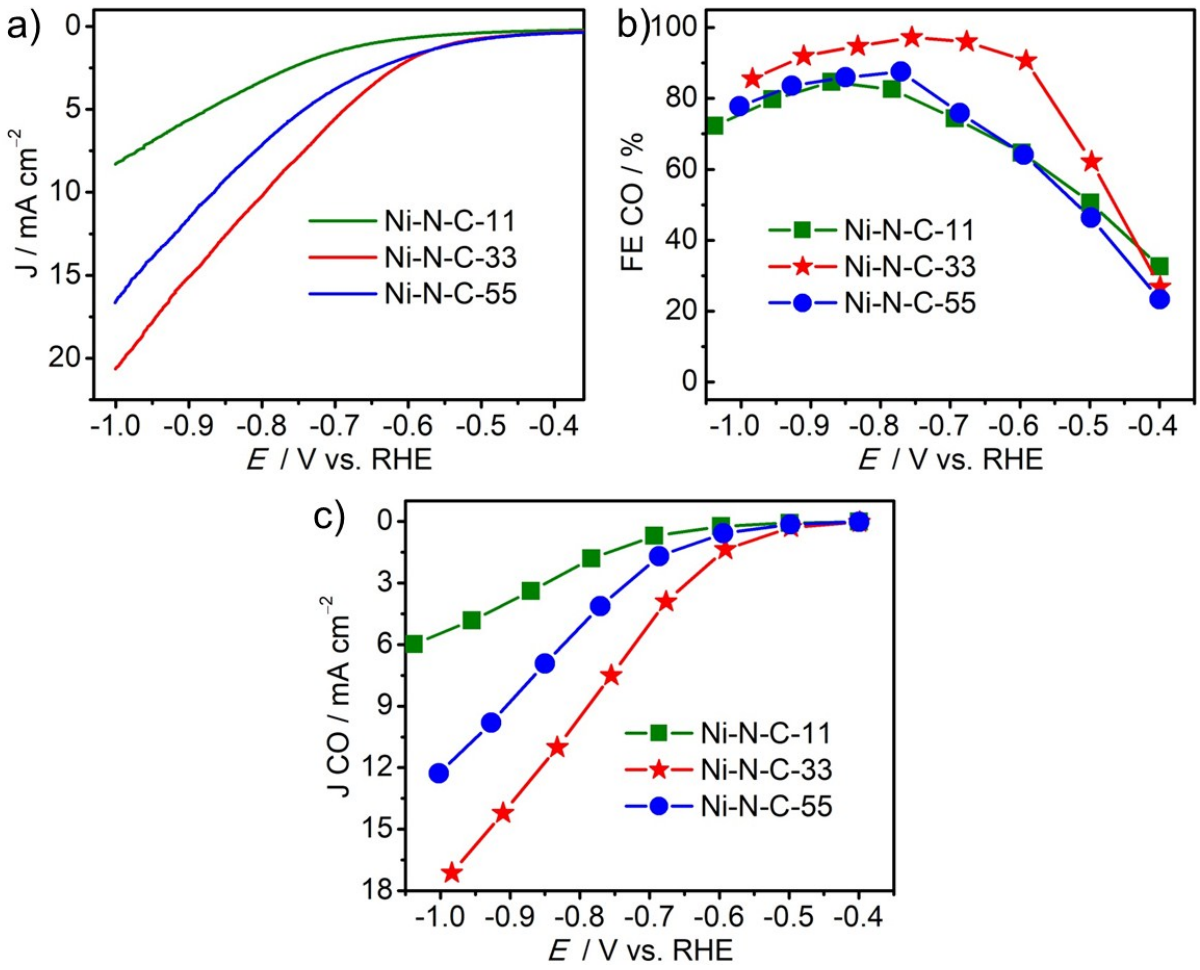


**Fig. S3.** Optimization of Ni-N-C activity by adjusting Ni percentage in the total metal (Ni+Zn) from 11% (Ni-N-C-11), 33% (Ni-N-C-33) and 55% (Ni-N-C-55) in preparing Ni-doped ZIF.

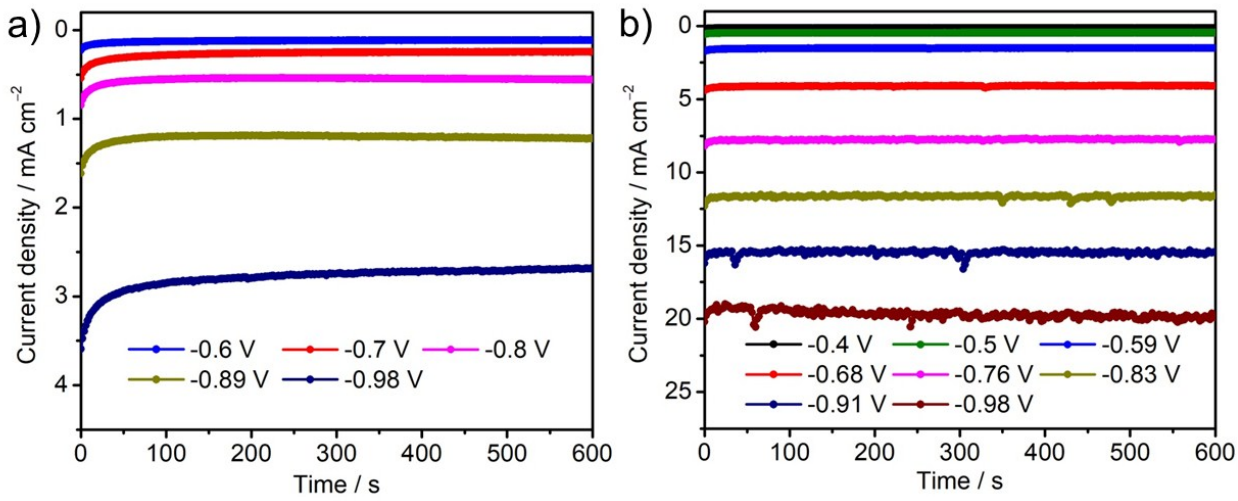


**Fig. S4.** 10 min continuous chronoamperometric experiments for $CO_2$RR at different applied potentials on (a) N-C, (b) Ni-N-C.

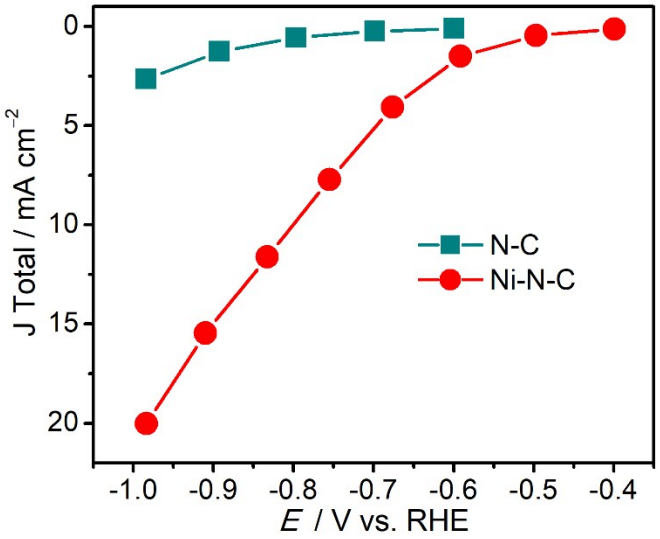


**Fig. S5.** Total current density of N-C and Ni-N-C.

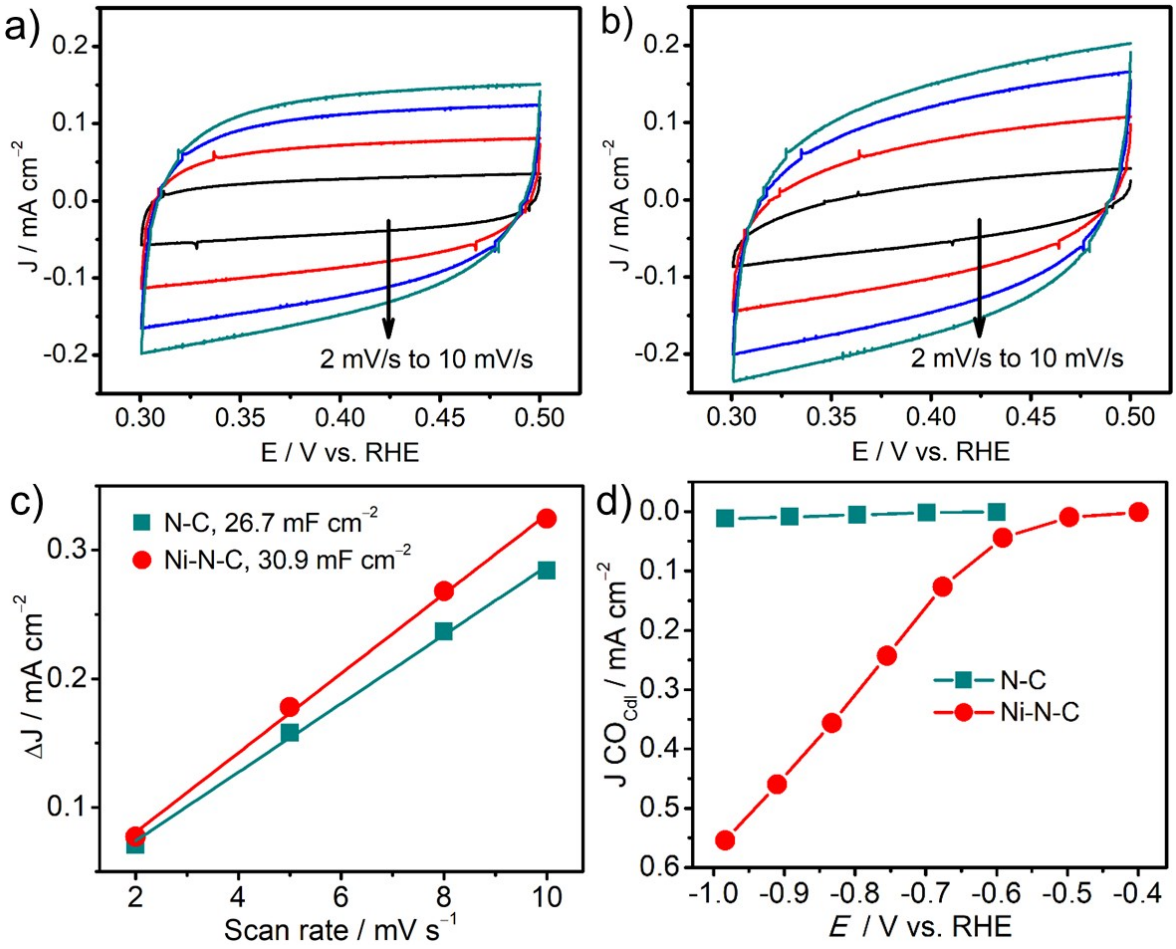


**Fig. S6.** Cyclic voltammetry conducted in $CO_2$-saturated 0.1 M $KHCO_3$ solution at scan rate 2, 5, 8, and 10 15 mV $s^{-1}$ for N-C (a) and Ni-N-C (b). (c) charging current density differences plotted against scan rates and (d) CO partial current density normalized to $C_{dl}$ for N-C and Ni-N-C.

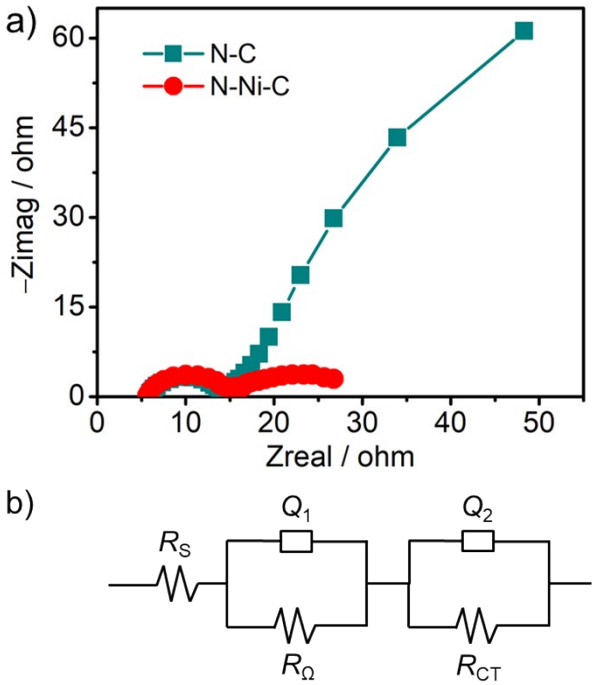


| Catalyst | $R_S$ (Ω) | $R_\Omega$ (Ω) | $R_{CT}$ Ω) |
|---|---|---|---|
| N-C | 5.8 | 8.9 | 652.4 |
| Ni-N-C | 5.6 | 8.6 | 18.1 |

**Fig. S7.** (a) An equivalent circuit model and parameter values of the equivalent circuits calculated by simulations. In the equivalent circuit, $R_S$ is the solution resistance, $R_\Omega$ is the ohmic resistance, Rct is the charge transfer resistance, and Q is the constant phase element.

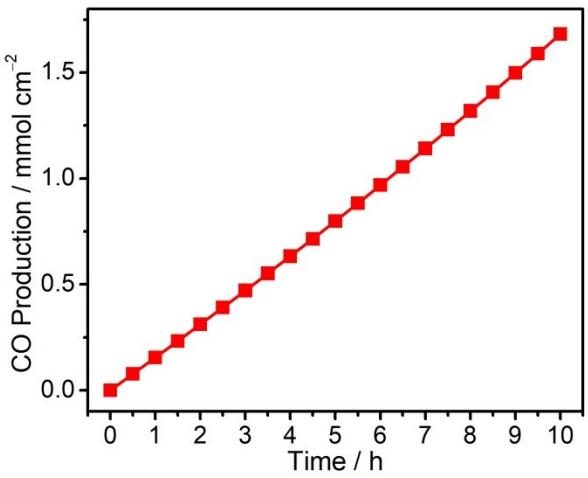


**Fig. S8.** Total production of CO on Ni-N-C at an applied potential of −0.75 V for 10 h tests.

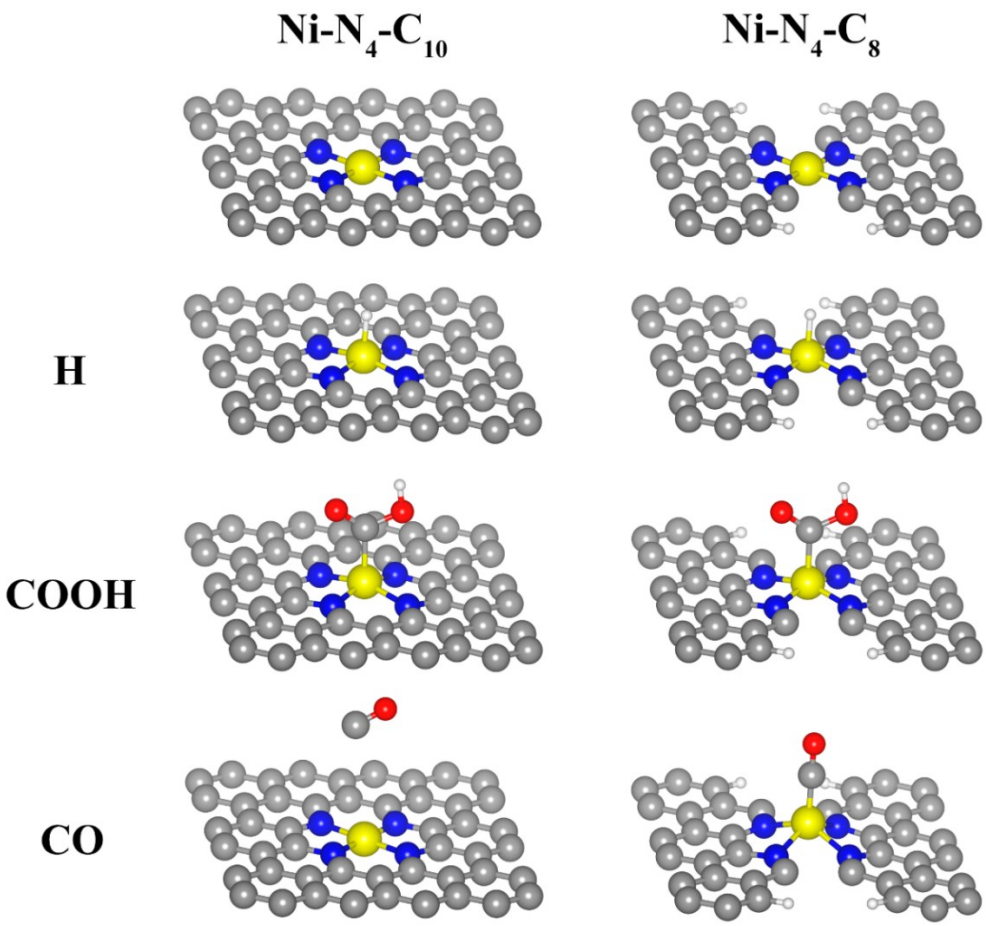


**Fig. S9.** The atomic structures and adsorption configurations for H, COOH and CO on modeled Ni-$N_4$-$C_{10}$ and Ni-$N_{2+2}$-$C_8$ active sites. In the figure, the gray, blue, yellow, red, and white balls represent C, N, Ni, O, and H atoms, respectively. Note: the CO molecule desorb spontaneously from the Ni-$N_4$-$C_{10}$ active site.

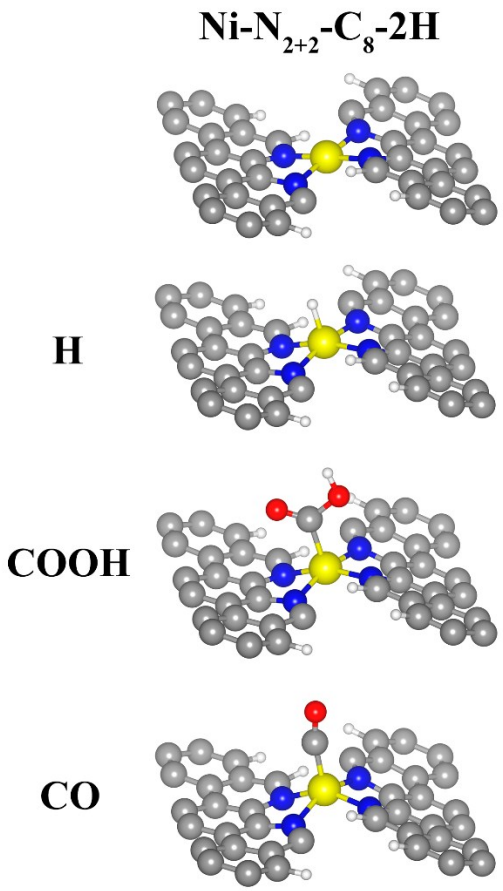


**Fig. S10.** The atomic structures and adsorption configurations for H, COOH and CO on modeled Ni-$N_{2+2}$-$C_8$ active sites with 2 dangling bonds passivated by hydrogen atoms. In the figure, the gray, blue, yellow, red, and white balls represent C, N, Ni, O, and H atoms, respectively.

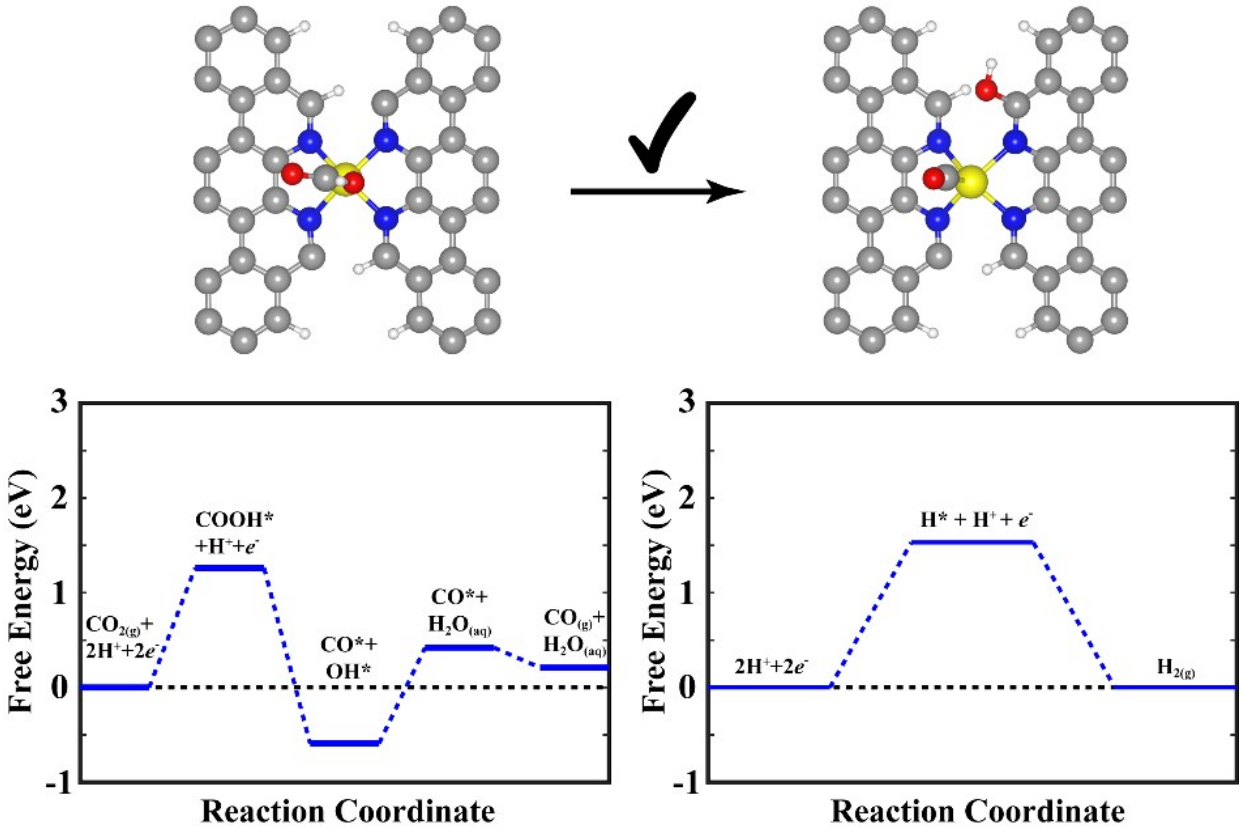


**Fig. S11.** The initial and final state for the COOH dissociation reaction on Ni−$N_{2+2}$-$C_8$-2H site. Calculated free energy evolution of $CO_2$ reduction to CO, and hydrogen evolution reaction on applied electrode potential (U) of 0 V.

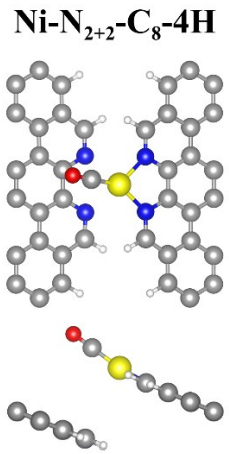


**Fig. S12.** The adsorption configuration for CO on modeled Ni-$N_{2+2}$-$C_8$ active sites with 4 dangling bonds passivated by hydrogen. Top panel: top view; bottom panel: side view.

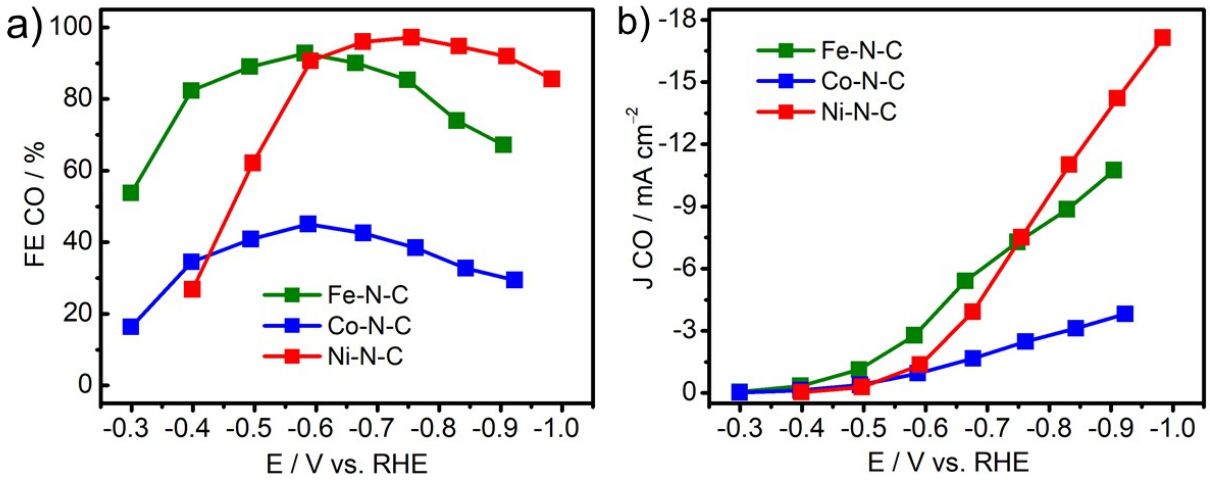


**Fig. S13.** (a) FEs and (b) partial current density comparisons between Ni-N-C, Co-N-C, and Fe-N-C. These three catalysts were prepared using the same method and conditions. The results of Co-N-C and Fe-N-C were previously published in ACS Catalysis 2018, 8, 3116.

**Table S1.** Comparison of $CO_2RR$ performances for CO production between Ni-N-C in this work and reported typical Ni-N-C catalysts.

| Catalysts | Con. of $KHCO_3$ | FE CO [a] (%) | $J_{CO}$ [b] (mA $cm^{-2}$) | η [c] (mV) | References |
|---|---|---|---|---|---|
| **Ni-N-C** | 0.1 | 97 | 7.5 | 640 | This work |
| **Ni SAs/N-C** | 0.1 | 72 | 10.5 | 890 | *J. Am. Chem. Soc.*, 2017, 139, 8078-8081 |
| **Ni-$N_4$-C** | 0.5 | 99 | 28.6 | 700 | *J. Am. Chem. Soc.*, 2017, 139, 14889-14892. |
| **Ni-N-C layers** | 0.5 | 96 | 8.4 | 650 | *Appl. Catal. B: Environ.*, 2018, 226, 463-472 |
| **Fe-N-CB** | 0.5 | 95 | 11 | 620 | *Energy Environ. Sci.*, 2018, 11, 893-903 |
| **Ni-N-Ketjen600EC** | 0.1 | 85 | 13 | 710 | *Energy Environ. Sci.*, 2019, 12, 640-647 |
| **A-Ni-NG** | 0.5 | 97 | 22 | 610 | *Nat. Energy*, 2018, 3, 140-147 |
| **Ni-N-porous carbon** | 0.1 | 83 | 10 | 640 | *Nat. Commun.*, 2017, 8, 944. |

[a] The maximum FE for CO production;

[b] CO partial current density at the potential where the maximum FE is obtained;

[c] Overpotential at which the maximum FE is obtained.

**Table S2.** Predicted onset potential vs. RHE for $CO_2$ reduction to CO ($V_{CO2RR}$), onset potential vs. RHE for hydrogen evolution ($V_{HER}$), and heats of reaction for COOH dissociation to CO and OH ($\Delta H_0$) on various active sites.

| Active sites | Ni-$N_4$-$C_{10}$ | Ni-$N_{2+2}$-$C_8$ |
|---|---|---|
| $V_{CO2RR}$ (V) | -1.51 | -1.19 |
| $V_{HER}$ (V) | -1.70 | -1.43 |
| $\Delta H_0$ (eV) | 1.48 | -1.22 |

**Table S3.** Calculated electronic energy, ZPE, enthalpic temperature correction, entropy, solvation correction, and free energy of each CO2RR intermediate at 0 V (vs. RHE). The calculation of relative free energy uses $CO_2$(g), $H_2$(g) and $H_2O$(aq) as the reference states.

| | Species | Electronic Energy (eV) | ZPE (eV) | $\int_0^T C_p dT$ (eV) | Entropy (eV) | Solvation Correction (eV) | Free Energy (eV) | Relative Free Energy (eV) |
|---|---|---|---|---|---|---|---|---|
| Ni-$N_4$-$C_{10}$ | Site | -264.81 | - | - | - | - | - | - |
| | COOH* | -289.155 | 0.61 | 0.111 | 0.261 | -0.25 | -24.14 | 1.51 |
| | CO* | -279.273 | 0.21 | 0.064 | 0.141 | -0.1 | -14.43 | 0.58 |
| | H* | -266.824 | 0.21 | 0.01 | 0.01 | 0 | -1.8 | 1.70 |
| Ni-$N_{2+2}$-$C_8$ | Site | -341.33 | - | - | - | - | - | - |
| | COOH* | -365.991 | 0.61 | 0.111 | 0.261 | -0.25 | -24.45 | 1.19 |
| | CO* | -356.229 | 0.21 | 0.064 | 0.141 | -0.1 | -14.87 | 0.14 |
| | H* | -343.619 | 0.21 | 0.01 | 0.01 | 0 | -2.08 | 1.43 |

## References


1. G. Kresse and J. Hafner, *Phys. Rev. B*, 1994, **49**, 14251-14269.
2. G. Kresse and D. Joubert, *Phys. Rev. B*, 1999, **59**, 1758-1775.
3. B. Hammer, L. B. Hansen and J. K. Nørskov, *Phys. Rev. B*, 1999, **59**, 7413-7421.
4. J. K. Nørskov, J. Rossmeisl, A. Logadottir, L. Lindqvist, J. R. Kitchin, T. Bligaard and H. Jonsson, *J. Phys. Chem B.*, 2004, **108**, 17886-17892.
5. H. Afeefy, J. Liebman and S. Stein, *Neutral thermochemical data*, National Institute of Standards and Technology, Gaithersburg, MD, USA, 2010.
6. A. A. Peterson, F. Abild-Pedersen, F. Studt, J. Rossmeisl and J. K. Norskov, *Energ. Environ. Sci.*, 2010, **3**, 1311-1315.
7. V. Tripkovic, M. Vanin, M. Karamad, M. E. Bjorketun, K. W. Jacobsen, K. S. Thygesen and J. Rossmeisl, *J. Phys. Chem. C*, 2013, **117**, 9187-9195.